Nanoscale Research Letters

NANO EXPRESS Open Access

# Enhancing Water-Splitting Efficiency Using a Zn/Sn-Doped PN Photoelectrode of Pseudocubic α-$Fe_2O_3$ Nanoparticles

Jie-Xiang Yang[1,2†], Yongtao Meng[3†], Chuan-Ming Tseng[4,5*], Yan-Kai Huang[4], Tung-Ming Lin[1,2], Yang-Ming Wang[1,2], Jin-Pei Deng[6], Hsiang-Chiu Wu[7] and Wei-Hsuan Hung[1,8*]

## Abstract

α-Phase hematite photoelectrodes can split water. This material is nontoxic, inexpensive, and chemically stable; its low energy gap of 2.3 eV absorbs light with wavelengths lower than 550 nm, accounting for approximately 30% of solar energy. Previously, we reported polyhedral pseudocubic α-$Fe_2O_3$ nanocrystals using a facile hydrothermal route to increase spatial charge separation, enhancing the photocurrent of photocatalytic activity in the water-splitting process. Here, we propose a p-n junction structure in the photoanode of pseudocubic α-$Fe_2O_3$ to improve short carrier diffusion length, which limits its photocatalytic efficiency. We dope Zn on top of an $Fe_2O_3$ photoanode to form a layer of p-type semiconductor material; Sn is doped from the FTO substrate to form a layer of n-type semiconductor material. The p-n junction, n-type $Fe_2O_3$:Sn and p-type $Fe_2O_3$:Zn, increase light absorption and charge separation caused by the internal electric field in the p-n junction.

**Keywords:** Pseudocubic α-$Fe_2O_3$, Water splitting, p-n junction, Solar energy

## Introduction

To build a sustainable, renewable, and clean energy economy, solar-driven photoelectrochemical (PEC) water-splitting offers a promising route for effective solar fuel production. Most semiconductor materials possess reasonable sunlight absorption and conversion efficiencies as well as active catalytic properties; thus, they are strong candidates for photoelectrodes. Notably, hematite has attracted much attention because of its nontoxicity, high chemical stability, environmental compatibility, low cost, and low energy gap of 2.3 eV, which can effectively absorb wavelengths of less than 550 nm of visible light [1–5]. However, the PEC performance for water oxidation on α-$Fe_2O_3$ photoanodes [6, 7] is limited by their poor charge conductivity [8, 9] and mobility [10, 11], low absorption coefficient [8, 12], and rapid electron-hole recombination [13–15], which depresses the oxygen evolution reaction. To address these limitations, numerous approaches have focused on enhancing light absorption, the kinetics of the water oxidation reaction, and the charge-carrier collection efficiency through modifying electronic structural elements. For example, some studies have reported that introducing several types of ions into hematite could significantly improve the hematite carrier concentration and charge transfer rate at the surface [16–18]. In our previous study, we proposed facilitating the preferential migration of electrons and holes in semiconductors using differences in work functions at various crystal facets, which improved the spontaneous charge spatial separation during the water-splitting process [1, 19, 20]. In the present study, we sought to go further to improve the performance of water splitting based on the results of our previous study, combining the advantages of the existence of heteroions in

* Correspondence: cmtseng@mail.mcut.edu.tw; hungwh@ncu.edu.tw
†Jie-Xiang Yang and Yongtao Meng contributed equally to this work.
[4]Department of Materials Engineering, Ming Chi University of Technology, New Taipei City 24301, Taiwan
[1]Institute of Materials Science and Engineering, National Central University, Taoyuan 32001, Taiwan
Full list of author information is available at the end of the article

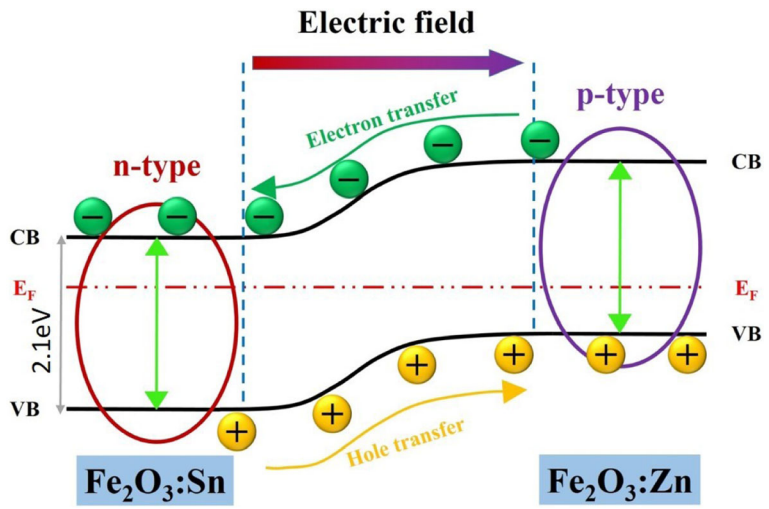


**Fig. 1** Concept of the p-n junction in a photoelectrode of polyhedral pseudocubic α-$Fe_2O_3$

photoanodes. Two types of ions, Zn and Sn, were incorporated into a layer of shaped controlled hematite cubes from the top and bottom, respectively, which also created concentration gradience differences in the two types of ions within the active layer of hematite (Fig. 1). In our previous study, Sn doping occurred spontaneously from the FTO substrate during the post-annealing process, and Zn doping was performed by spin-coating precursors of zinc acetate solution on the top surface of photoanodes and thermally reduced during post-annealing; this modified the flat-band potential at the semiconductor-electrolyte interface.

## Methods

Pseudocubic α-$Fe_2O_3$ nanocrystals were prepared through a hydrothermal route. In the synthesis of (012)-pseudocubic α-$Fe_2O_3$ nanocrystals, precursor $Fe(acac)_3$ (2 mmol) and aqueous NaOH (0.6 M, 20 mL) were sequentially added to a solution of ethanol (20 mL) and DI-water (20 mL) with homogeneously vigorous stirring. Next, the mixed solution was placed in a Teflon-lined autoclave (100 mL) and maintained at 180 °C for 24 h. After being cooled to room temperature, the products were collected by centrifugation at 8000 rpm for 3 min and washed several times with n-hexane.

Subsequently, the products were ground into a powder and mixed with n-propyl ethanol (5 mL of n-propyl ethanol/0.1 g of powder) to obtain a suspension. In the doping process of Zn, we mixed zinc acetate and ethanol (0.1 g of zinc acetate + 2 mL of ethanol) to obtain zinc acetate solution. Finally, the pseudocubic α-$Fe_2O_3$ photoelectrodes were prepared using a spin-coating method and sintered at 450 °C for 10 h (heating rate = 2.5 °C/min) on the FTO substrate. In addition, Zn doping was prepared with a thermal diffusion method. We mixed zinc acetate and ethanol (0.1 g of zinc acetate + 2 ml of 99.5% ethanol) to obtain zinc acetate solution, which was then dropped 200 μL onto the pseudocubic α-$Fe_2O_3$ film. The active area of each sample was 1 × 1 $cm^2$, and the mass loading of the $Fe_2O_3$ was approximately 0.2 mg. The prepared photoanode sintered at 450 °C for 10 h (heating rate = 2.5 °C/min) on the FTO substrate.

Characterizations of the pseudocubic $Fe_2O_3$ photoelectrode were performed using a field-emission scanning electron microscope (FE-SEM; S-4800, Hitachi) and high-resolution transmission electron microscope (HR-TEM; JEM-2100, JEOL). TEM samples were prepared by drop-casting an ethanol suspension of pseudocubic $Fe_2O_3$ NPs onto a copper grid. The composition and crystallinity of this $Fe_2O_3$ photoelectrode were determined using X-ray diffraction (XRD; D8 SSS Bruker). To study improvements to the separation of photoinduced charges, photoluminescence (PL) spectroscopy was performed to examine the recombination rate of photogenerated electron-hole pairs. The photon absorption properties of polyhedral α-$Fe_2O_3$ nanocrystals and their plasmon resonance were observed using ultraviolet-visible spectroscopy (UV-Vis; Lambda 650S, PerkinElmer). Photoelectrochemicals were measured using an electrochemical analyzer (CHI 6273E, CH Instruments) with a three-electrode electrochemical cell system in a darkroom (working electrode: hematite thin films, reference electrode: Ag/AgCl, counter electrode: carbon rod). The electrolyte was 1 M NaOH (pH = 14). In the photoelectrochemical measurement process, the light source was 532-nm laser irradiation (green solid laser, ALPHA-LAS) with a calibrated power density of 320 $mW/mm^2$ with a spot size 1 mm in diameter. Hydrogen production was measured using gas chromatography (GC, China

Chromatography GC1000TCD). Furthermore, the gas product was sampled every 20 min for 2 h.

## Results and Discussion

Figure 2 presents TEM images of the α-$Fe_2O_3$, which indicate that the obtained particles possessed a pseudocubic shape and measured approximately 20 nm. The pseudocubic α-$Fe_2O_3$ consisted of (012) and (112) facets, and the crystallographic orientation was determined through the FFT pattern and high-resolution TEM images shown in Fig. 2b and c. These pseudocubic nanocrystals had an oblique parallelepiped morphology, where the dihedral angle between two adjacent facets was 86° or 94°. The FFT diffraction pattern shows that the (012) and (112) planes were nearest, and the interplanar distance was indicated as 3.7 Å along the [012] direction.

Figure 3 presents the XPS spectra of pseudocubic-$Fe_2O_3$:Zn/Sn for examining their chemical bonding state and electron bonding energy. In Fig. 3a, the presence of Zn in a-$Fe_2O_3$ was exhibited in the XPS spectrum, in which the peaks located at 1020.6 and 1044.1 eV were related to Zn 2p3/2 and Zn 2p1/2, respectively. In Fig. 3c, the high-resolution Zn 2p spectrum exhibits a pronounced peak centered at 1021.8 eV, corresponding to Zn 2p3/2, where the binding energy of Zn 2p3/2 is the typical value for ZnO; this suggested that the Zn dopant existed in the form of $Zn^{2+}$. Zn was proved to be successfully doped within the $Fe_2O_3$. According to Fig. 3b, the XPS spectrum of Fe 2p3/2 and Fe2p1/2 in the Zn in a-$Fe_2O_3$ could be fitted as peaks at 710.7 and 724.3 eV, which was consistent with the binding energy of $Fe^{3+}$ in the $Fe_2O_3$ origin.

Figure 4a–f shows a scanning transmission electron microscope with high-angle annular dark field (STEM-HAADF) cross-section micrograph of a Zn/Sn-doped PN pseudocubic $Fe_2O_3$ photoelectrode on an FTO-coated glass substrate. For protection purposes, Pt was coated onto the surface of the hematite film during the preparation of the TEM sample. Energy-dispersive spectroscopy (EDS) elemental maps of the Zn, Fe, Sn, and Si elemental distributions are shown in Fig. 4b–f, respectively. The pseudocubic $Fe_2O_3$ NPs could be observed to cover the FTO-coated substrate conformably. To examine the doping concentration distribution in depth, we performed an XPS depth scan. Figure 4 g depicts the atomic percentage (at%) of the elemental distributions as a function of sputter time for the pseudocubic-$Fe_2O_3$:Zn/Sn photoelectrode, along with a schematic representation of each layer. In this concentration depth profile, we observed the Zn 2p to exhibit the highest concentration at the top surface (approx. 20%), which decreased with sputter time. In addition, Sn diffusion from the FTO substrate was observed in our photoelectrode, which intercrossed with the Zn signal line at a sputter time of 50 min. The perfect spatial distribution of both Zn and Sn demonstrated a successful doping atom arrangement in the Zn/Sn-doped PN pseudocubic $Fe_2O_3$ photoelectrode. This result contributed toward an enhancement of the reaction photocurrent.

To identify the effect of pseudocubic $Fe_2O_3$:Sn with and without Zn doping, the absorption spectra of the

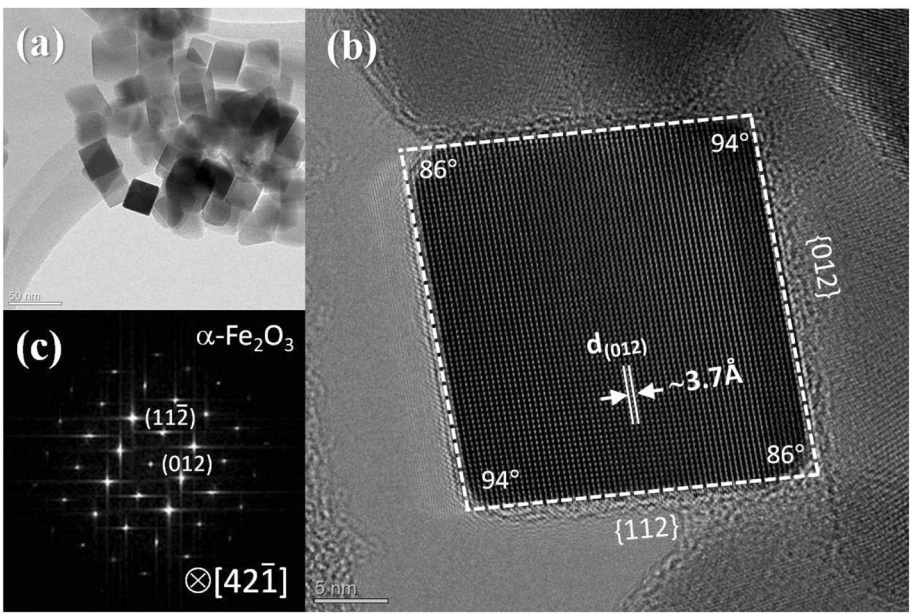


**Fig. 2** **a** TEM image of pseudocubic-$Fe_2O_3$ NPs. **b** High-resolution TEM image of a pseudocubic-$Fe_2O_3$ NP. **c** The FFT pattern in **b** reveals an α-$Fe_2O_3$ NP along its [42$\bar{1}$] projection

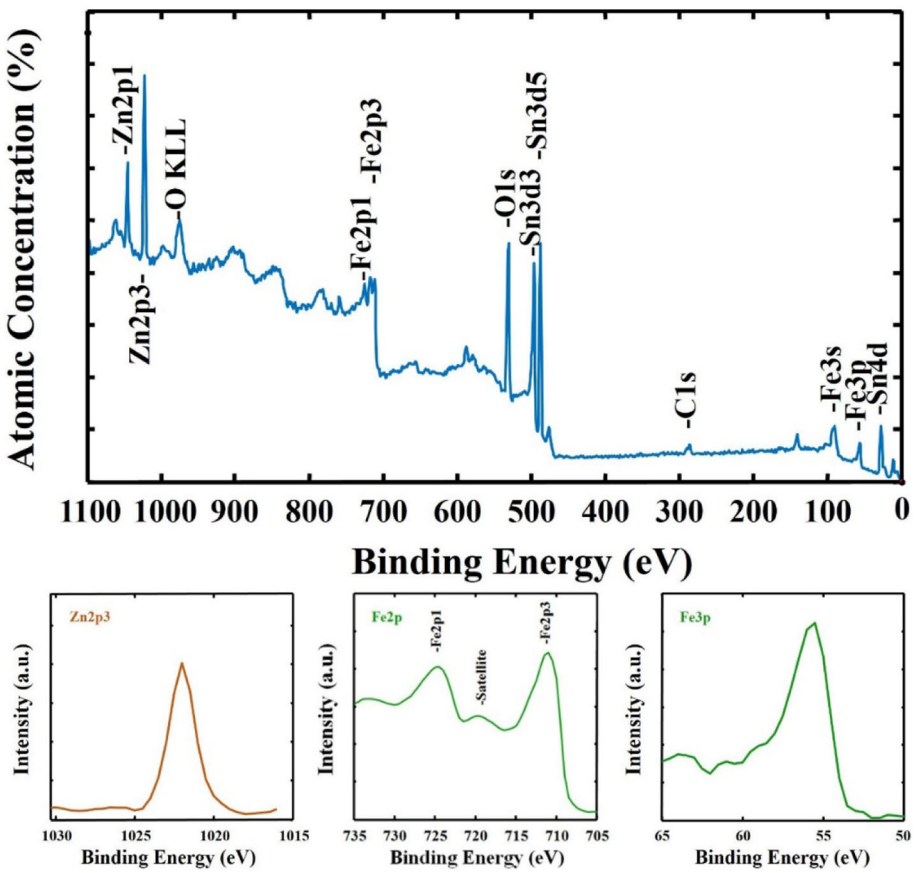


**Fig. 3** X-ray photoelectron spectroscopy (XPS) analysis of the Zn/Sn-doped p-n pseudocubic $Fe_2O_3$ photoelectrode: **a** survey XPS spectrum; **b** Fe 2*p*; and **c** Zn 2*p*

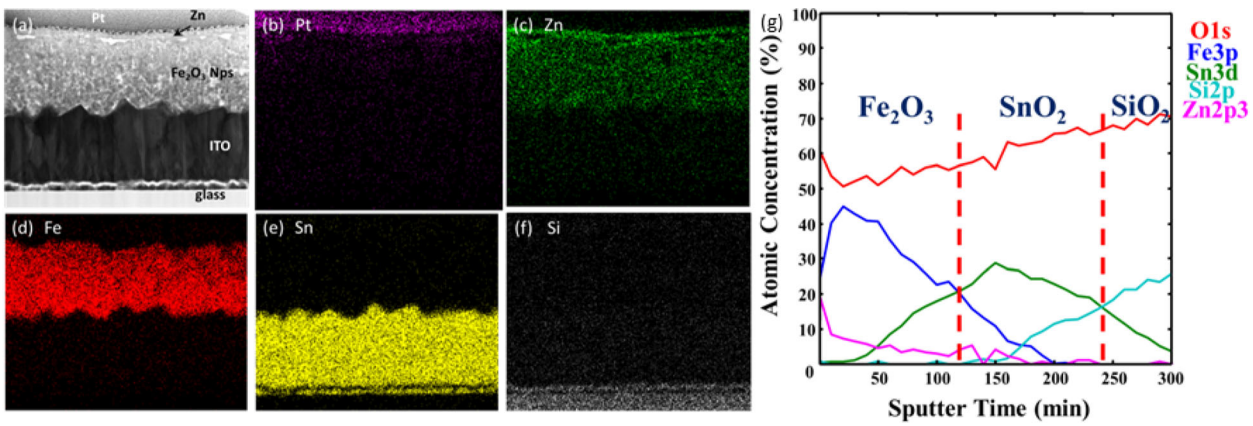


**Fig. 4** Cross-sectional imaging and chemical mapping of Zn/Sn-doped p-n pseudocubic $Fe_2O_3$ photoelectrode: **a**–**f** STEM images of the cross-section of an Zn/Sn-doped PN pseudocubic $Fe_2O_3$ photoelectrode. Note that the thin Pt layer seen in the image was deposited over the sample as a protection layer for the focused ion beam (FIB) milling step for cross-sectional sample preparation. **g** EDS mapping showing Zn, Fe, Sn, and Si elemental distributions respectively for the same sample as in **a**

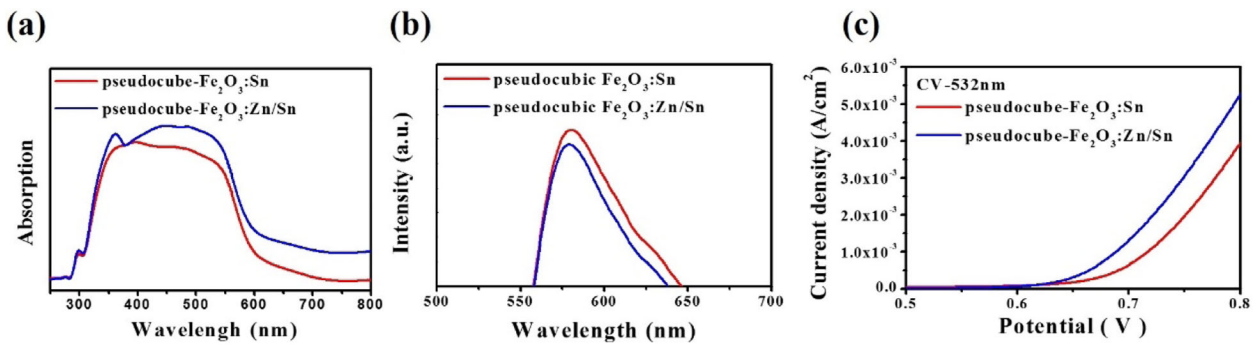


**Fig. 5** **a** Absorption spectrum of the photoelectrodes of $Fe_2O_3$:Sn and $Fe_2O_3$:Zn/Sn; **b** PL analysis of the $Fe_2O_3$:Sn and $Fe_2O_3$:Zn/Sn photoelectrodes; and **c** J-V scans collected for different doped $Fe_2O_3$

$Fe_2O_3$:Sn and $Fe_2O_3$:Zn/Sn photoelectrodes were measured, as shown in Fig. 5a. The absorption spectrum of the $Fe_2O_3$:Zn/Sn (p-n junction) photoelectrode exhibited a stronger photon absorption crossover in the UV-to-visible light range. In addition, a small bump of an absorption peak appearing at 440 nm was observed; this was consistent with the absorption peak of the Zn NPs, which was because of the substitution between zinc and iron atoms [21–23]. Notably, a slight blue shift phenomenon was observed in the absorption spectrum after the Zn NPs were doped in the pseudocubic $Fe_2O_3$:Sn photoelectrode [24–26]. This phenomenon may be attributable to the Zn NP doping possibly raising the band gap of essential semiconductors [27–31]. Moreover, Mott-Schottky plot is performed for Zn/Sn -doped PN photoelectrode of pseudocubic α-$Fe_2O_3$ and have been characterized in Figure S1 in the supporting information. In the case of Zn/Sn-doped pseudocubic α-$Fe_2O_3$, it has been noted that both positive and negative slopes are observed, implying that the existence of the p and n type electronic behavior in our photoelectrode (shown in supporting information, Figure S2).

To further investigate the charge transfer of the photogenerated electron and hole pairs in pseudocubic $Fe_2O_3$:Zn/Sn, p-n junction system, this study used photoluminescence (PL) analysis, which could indicate the recombination of free charge carriers. Figure 5b shows the PL spectra of different samples with an excitation wavelength of 263 nm (4.71 eV). The pseudocubic $Fe_2O_3$:Zn/Sn displayed a lower PL intensity at approximately 580 nm, which was because of carrier diffusion between the p- and n-type semiconductor materials. This implied a decrease in electron and hole pair recombination, attributed to the p-n junction internal electric field.

Photocurrent responses were measured using a traditional three-electrode cell system. It was designed in a

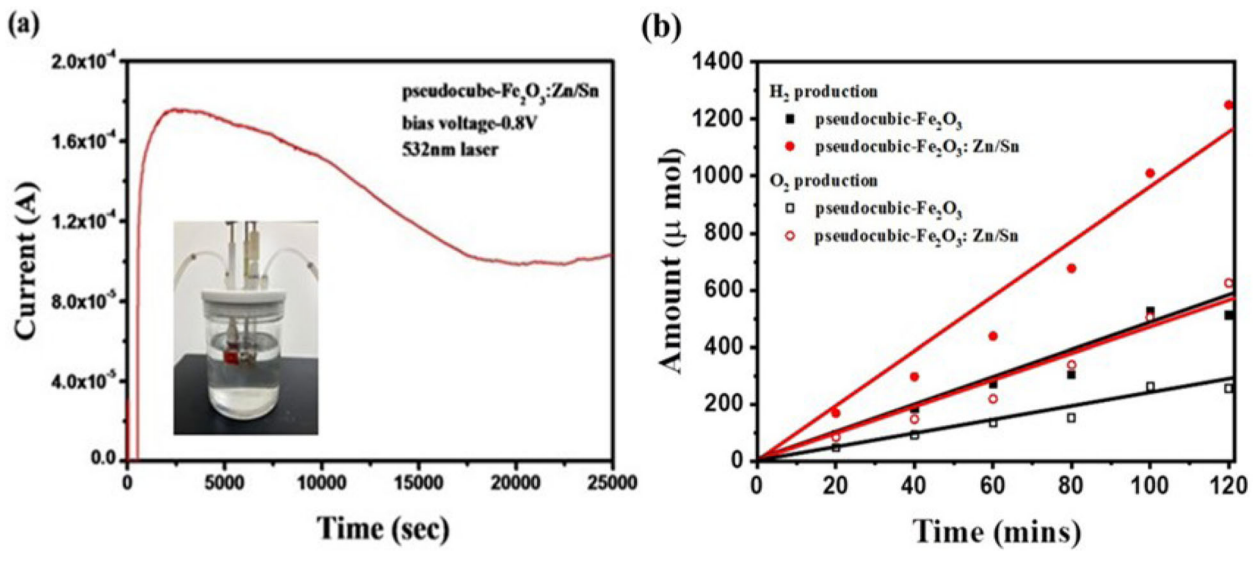


**Fig. 6** **a** Stability study of pseudocubic $Fe_2O_3$:Zn/Sn photoelectrodes (inset photo: our test system). **b** Production of $H_2$ and $O_2$ from pseudocubic $Fe_2O_3$:Zn/Sn photoelectrodes

quartz cell, in which hematite thin films were used as the working electrode, Ag/AgCl as a reference, and a carbon rod as a counter electrode. The electrolyte was 1 M NaOH (pH = 14). In Fig. 5c, two different photoelectrodes with and without Zn doped, respectively, were tested under 532-nm laser irradiation. The pseudocubic $Fe_2O_3$:Sn and $Fe_2O_3$:Zn/Sn exhibited photocurrent densities of $4.1 \times 10^{-3}$ and $5.3 \times 10^{-3}$ A/cm$^2$, respectively, at a bias voltage of 0.8 V. As expected, with superior performance in terms of the absorption spectrum and PL, the photocurrent-voltage (J-V) response of the pseudocubic $Fe_2O_3$:Zn/Sn (photocurrent density = 5.22 mA/cm$^2$) was approximately 30% higher than that of the pseudocubic $Fe_2O_3$:Sn under 532-nm laser irradiation.

The long-term stability of the $Fe_2O_3$:Zn/Sn photoelectrodes was tested under 532-nm laser irradiation for 7 h in Fig. 6a. The p-n junction system achieved a high light current response in a previous measurement. After irradiation for 7 h, the current response of the $Fe_2O_3$:Zn/Sn photoelectrode had only decayed by 35%, which confirmed that the Zn/Sn-doped PN pseudocubic $Fe_2O_3$ photoelectrode possessed strong photocurrent response stability. Finally, we examined $H_2$ and $O_2$ production to demonstrate a possible application of this high-performance PN photoelectrode; a comparison of $H_2$ and $O_2$ production from water-splitting was conducted and is presented in Fig. 6b for both the $Fe_2O_3$:Sn and $Fe_2O_3$:Zn/Sn samples. The $Fe_2O_3$:Zn/Sn photoelectrode generated approximately 1200 μmol of $H_2$ and 520 μmol of $O_2$ in 120 min, which were two times greater than those of pseudocubic $Fe_2O_3$:Sn.

## Conclusions

This study successfully demonstrated an enhanced charge spatial separation effect in pseudocubic $Fe_2O_3$:Zn/Sn photoelectrodes, which significantly improved performance in terms of photocurrent response and water-splitting gas products because of the built-in electric field. Furthermore, the $Fe_2O_3$:Zn/Sn photoelectrodes exhibited promising long-term stability, remaining at 70% magnitude of the initial photocurrent over 7 h of operation. This provides a significant water-splitting approach for sustainable energy conversion.

## Supplementary information

**Supplementary information** accompanies this paper at https://doi.org/10.1186/s11671-020-03362-5.

**Additional file 1: Figure S1**. Mott-Schottky plot of the Zn/Sn doped PN photoelectrode of pseudocubic α-$Fe_2O_3$. **Figure S2**. The comparison of XRD before/after operation.

### Abbreviations

NP: Nanoparticle; PEC: Photoelectrochemical; FTO: Fluorine-doped tin oxide-coated glass; FE-SEM: Field-emission scanning electron microscope; HR-TEM: High-resolution transmission electron microscope; XRD: X-ray diffraction; PL: Photoluminescence; UV-Vis: Ultraviolet-visible spectroscopy; GC: Gas chromatography; XPS: X-ray photoelectron spectroscopy; EDS: Energy-dispersive spectroscopy; FIB: Focused ion beam; STEM-HAADF: High-angle annular dark field

### Acknowledgements

This work was financially supported by the "High Entropy Materials Center" from The Featured Areas Research Center Program within the framework of the Higher Education Sprout Project by the Ministry of Education (MOE) and from the Project MOST 108-3017-F-007-002-, 108-3116-F-008-008- (Dr. Wei-Hsuan Hung), 108-2218-E-011-008-, and 107-2218-E-131-004-MY3 (Dr. Chuan-Ming Tseng) by the Ministry of Science and Technology (MOST) in Taiwan.

### Authors' Contributions

J.X.Y., Y.T.M., Y.M.W., C.M.T., and W.H.H. designed the research; Y.K.H., T.M.L., J.P.D., H.C.W., C.M.T., and W.H.H. performed the research; C.M.T. and W.H.H. wrote the paper. All authors read and approved the final manuscript.

### Availability of Data and Materials

All data generated or analyzed during this study are included in this published article.

### Competing Interest

The authors declare that they have no competing interests.

### Author details

[1]Institute of Materials Science and Engineering, National Central University, Taoyuan 32001, Taiwan. [2]Department of Materials Science and Engineering, Feng Chia University, Taichung 40724, Taiwan. [3]College of Electrical Engineering and Automation, Shandong University of Science and Technology, Qingdao 266590, China. [4]Department of Materials Engineering, Ming Chi University of Technology, New Taipei City 24301, Taiwan. [5]Center for Plasma and Thin Film Technologies, Ming Chi University of Technology, New Taipei City 24301, Taiwan. [6]Department of Chemistry, Tamkang University, New Taipei City 25137, Taiwan. [7]Department of Mechanical Engineering, National Chung Cheng University, Chiayi 621301, Taiwan. [8]High Entropy Materials Center, National Tsing Hua University, Hsinchu 30013, Taiwan.

Received: 3 April 2020 Accepted: 1 June 2020
Published online: 15 June 2020

### References

1. Hung W-H et al (2016) Exploitation of a spontaneous spatial charge separation effect in plasmonic polyhedral α-Fe2O3 nanocrystal photoelectrodes for hydrogen production. Nano Energy 30:523–530
2. Le Formal F et al (2011) Passivating surface states on water splitting hematite photoanodes with alumina overlayers. Chem Sci 2(4):737–743
3. Tilley SD et al (2010) Light-induced water splitting with hematite: improved nanostructure and iridium oxide catalysis. Angew Chem Int Ed 49(36):6405–6408
4. Lin Y et al (2011) Hematite-based solar water splitting: challenges and opportunities. Energy Environ Sci 4(12):4862–4869
5. Tada H et al (2011) Titanium (IV) dioxide surface-modified with iron oxide as a visible light photocatalyst. Angew Chem Int Ed 50(15):3501–3505
6. Hung W-H et al (2014) Spatially controllable plasmon enhanced water splitting photocurrent in Au/TiO 2–Fe 2 O 3 cocatalyst system. RSC Adv 4(86):45710–45714
7. Hung W-H, Chien T-M, Tseng C-M (2014) Enhanced photocatalytic water splitting by plasmonic TiO2–Fe2O3 cocatalyst under visible light irradiation. J Phys Chem C 118(24):12676–12681
8. Wang J et al (2017) A facile electrochemical reduction method for improving photocatalytic performance of α-Fe2O3 photoanode for solar water splitting. ACS Appl Mater Interfaces 9(1):381–390
9. Annamalai A et al (2016) Fabrication of superior α-Fe2O3 nanorod photoanodes through ex-situ Sn-doping for solar water splitting. Sol Energy Mater Sol Cells 144:247–255
10. Moradlou O et al (2018) Carbon quantum dots as nano-scaffolds for α-Fe2O3 growth: preparation of Ti/CQD@ α-Fe2O3 photoanode for water splitting under visible light irradiation. Appl Catal B Environ 227:178–189

11. Segev G et al (2016) High solar flux concentration water splitting with hematite (α-Fe2O3) photoanodes. Adv Energy Mater 6(1):1500817
12. Xia L et al (2017) High-performance BiVO4 photoanodes cocatalyzed with an ultrathin α-Fe2O3 layer for photoelectrochemical application. Appl Catal B Environ 204:127–133
13. Carroll GM, Zhong DK, Gamelin DR (2015) Mechanistic insights into solar water oxidation by cobalt-phosphate-modified α-Fe 2 O 3 photoanodes. Energy Environ Sci 8(2):577–584
14. Carroll GM, Gamelin DR (2016) Kinetic analysis of photoelectrochemical water oxidation by mesostructured Co-Pi/α-Fe 2 O 3 photoanodes. J Mater Chem A 4(8):2986–2994
15. Xu Z et al (2018) Interface manipulation to improve plasmon-coupled photoelectrochemical water splitting on α-Fe2O3 photoanodes. ChemSusChem 11(1):237–244
16. Husek J et al (2017) Surface electron dynamics in hematite (α-Fe2O3): correlation between ultrafast surface electron trapping and small polaron formation. Chem Sci 8(12):8170–8178
17. Hajibabaei, H., Y. Gao, and T.W. Hamann, Unravelling the charge transfer mechanism in water splitting hematite photoanodes. Advances in Photoelectrochemical Water Splitting: Theory, Experiment and Systems Analysis, 2018(20): p. 100.
18. Chen Y et al (2018) ZIF-8 derived hexagonal-like α-Fe2O3/ZnO/Au nanoplates with tunable surface heterostructures for superior ethanol gas-sensing performance. Appl Surf Sci 439:649–659
19. Pan Q et al (2019) BiVO4 nanocrystals with controllable oxygen vacancies induced by Zn-doping coupled with graphene quantum dots for enhanced photoelectrochemical water splitting. Chem Eng J 372:399–407
20. Pan Q et al (2018) Boosting charge separation and transfer by plasmon-enhanced MoS2/BiVO4 p–n heterojunction composite for efficient photoelectrochemical water splitting. ACS Sustain Chem Eng 6(5):6378–6387
21. Sakamoto R et al (2017) Photofunctionality in porphyrin-hybridized bis (dipyrrinato) zinc (II) complex micro- and nanosheets. Angew Chem Int Ed 56(13):3526–3530
22. Hussain S et al (2019) Calculation of Judd Ofelt parameters: Sm3+ ions doped in zinc magnesium phosphate glasses. Solid State Commun
23. Lim GN, D'Souza F (2015) Multi-modular, tris (triphenylamine) zinc porphyrin–zinc phthalocyanine–fullerene conjugate as a broadband capturing, charge stabilizing, photosynthetic 'antenna-reaction center'mimic. Nanoscale 7(15):6813–6826
24. Iqbal S et al (2018) Effect of glycation on human serum albumin–zinc interaction: a biophysical study. JBIC Journal of Biological Inorganic Chemistry 23(3):447–458
25. Shi Y-X et al (2017) A crystalline zinc (II) complex showing hollow hexagonal tubular morphology evolution, selective dye absorption and unique response to UV irradiation. Chem Commun 53(40):5515–5518
26. Koutu V, Shastri L, Malik M (2017) Effect of temperature gradient on zinc oxide nano particles synthesized at low reaction temperatures. Materials Research Express 4(3):035011
27. Khan MM et al (2017) Microstructural properties and enhanced photocatalytic performance of Zn doped CeO 2 nanocrystals. Sci Rep 7(1): 12560
28. El-Hagary M et al (2018) Variations of energy band gap and magnetic properties upon quantum confinement effects on the Cr doped ZnO nanoparticles. Materials Research Express 6(1):015030
29. Rana S, Singh RP (2016) Investigation of structural, optical, magnetic properties and antibacterial activity of Ni-doped zinc oxide nanoparticles. J Mater Sci Mater Electron 27(9):9346–9355
30. Ahamed M et al (2016) Role of Zn doping in oxidative stress mediated cytotoxicity of TiO 2 nanoparticles in human breast cancer MCF-7 cells. Sci Rep 6:30196
31. Shakil A et al (2018) A Review on zinc sulphide thin film fabrication for various applications based on doping elements. Mater Sci Appl 9(09):751


## Publisher's Note